Microclimates in fumarole ice caves on volcanic edifices—Mount Rainier, Washington, USA

Lee J. Florea[*1], *Andreas Pflitsch*[†2], *Eddy Cartaya*[‡3], *Christian Stenner*[§4]

[1]Indiana Geological and Water Survey, Indiana University, Bloomington, Indiana, USA
[2]Ruhr-University Bochum, Bochum, Germany
[3]Glacier Cave Explorers, Redmond, Oregon, USA
[4]Alberta Speleological Society, Calgary, Alberta, Canada

Keywords: time-series analysis, wavelet analysis, cross correlation, glaciovolcanic caves, thermal flux

Highlights:

- Fumarole ice caves form from dynamic equilibrium between thermal flux, glacial movement, mass wasting, and meltwater recycling
- The scale and morphology of fumarole ice caves on Mount Rainier persists on decadal or longer scales.
- Heavy snowfalls seal cave entrances causing a positive feedback between rising cave air temperature and pressure and increased melt volume.

Data availability statement: Datasets for this research are available in an open-access archive hosted by the Indiana Geological and Water Survey and have been provided to Mt. Rainier National Park. Data archiving is underway.

Abstract

The fumarole ice caves of Mount Rainier in the Cascade Volcanic Arc in Washington, USA, provide unique insight into the dynamic equilibrium between thermal flux on volcanic edifices and snow accumulation on summit glaciers. More than 3.5 km of surveyed cave passage nearly circumnavigate the East Crater, reaching within 19 m of the 4392-m summit and extending to 144-m-deep along the glacier-crater boundary. The large circum-crater passage connects entrances on the crater rim to steep transverse passages, and cave morphology is maintained by fumarole gas convection and advection. A melt- and condensate-formed lake, Lake Adélie, occupies a portion of the circum-crater passage. Hourly data were collected between August 2016 and August 2017 and included the measured temperatures at three fumarole, the cave air temperature and pressure, the lake water temperature and depth, and the outside temperature and snow depth at Paradise Visitors Center. Time-series analyses of these data reveal complex associations between synoptic to seasonal weather, fumarole activity, and lake level. On seasonal and longer scales, fumarole temperatures follow independent pathways connected to spatial and temporal changes in volcanic heat flux and the circulation of glacial melt. For synoptic-scale meteorology, major snowfall seals the cave entrances, increasing cave air temperature and pressure from fumarole output and causing rising lake levels from increased melt until entrances reopen. Repeating freeze-thaw cycles observed in the cave monitoring data are a primary cause

[*] Corresponding author, lflorea@indiana.edu, (+1) 812-855-1376. Project PI for hydrology and geochemistry.
[†] Project PI for climate studies.
[‡] Permit holder and expedition leader.
[§] Chief project cartographer.

of crater mass wasting. Despite these variations, the scale and morphology of the caves is preserved over decadal or longer scales.

1. Introduction

Classic ice cave literature is oriented toward those bedrock caves that include perennial ice (Persoiu & Lauritzen, 2017, and references therein). In the literature on ice caves formed within glaciers, the process for conduit development is focused on flowing water, either through moulins or along the glacier base (Gulley et al., 2009). While air flow in ice caves and resulting ice melt has been investigated through the lens of 'cold-air traps' or the 'chimney effect' (Bertozzi et al., 2019; Luetscher & Jeannin, 2004; Meyer et al., 2016; Williams & McKay, 2015), these processes do not adequately describe systems that are formed entirely within ice and solely from advective air flow driven by temperature and pressure gradients at the ice-bedrock interface. Strictly speaking, this last category is glacio-thermo karst and is amplified in regions with increased geothermal gradient and, therefore, high heat flux. Specifically, these high heat flux regions are often volcanic settings—glaciovolcanic caves.

The speleogenesis of glaciovolcanic caves is one of thermal equilibrium. Heat flux creates melt, and on active volcanic edifices, this glacial melt percolates into the bedrock and undergoes a phase change to steam. Heat flux may be by conduction where the heated bedrock and ice are in contact (Giggenbach, 1976), but heat transfer by radiation and convection dominate where intervening melt-formed voids separate bedrock and ice.

Discrete fumaroles of steam and volcanic gas, as well as thermal springs, enhance cave formation; the size and shape of the 'fumarole ice cave' (Curtis & Kyle, 2011*; Pflitch et al., 2017*) is guided by the magnitude and locus of heat flux—larger cross sections form near concentrated fumarole and spring activity and greater heat transfer by convection (Kiver & Steele, 1975). The positive pressure gradient from fumarole activity causes lateral and vertical advection of steam and volcanic gas toward the glacial margins or moulins, which can enlarge and connect voids into conduits for moisture, volcanic gas, and heat transfer, such as on Mount Erebus in Antarctica (Wardell et al., 2003).

Thermal equilibrium and, therefore, advection through conduits in fumarole ice caves is modulated by short- and long-term changes in volcanic activity and external climate. Certainly, volcanism may rapidly eliminate all host ice on the edifice and lead to glaciovolcanism and features therein (Edwards et al., 2015; Tuffen et al., 2002). However, less extreme fluctuations in heat flux can significantly influence ice melt, fumarole activity, and thus, cave volume. Similarly, changes in atmospheric pressure and temperature may themselves effect advection, such as seasonal variations measured in the Fuji Ice Cave in Japan (Ohata et al., 1994), but more dramatically influence precipitation (i.e., snow) accumulation that can temporarily occlude the outlets for fumarole ice caves. Where the external climate is highly variable and subject to extreme events, such as in areas of higher altitude or precipitation, the impact can drive intra-annual volumetric changes within the fumarole caves.

Changes in melt volume and ice mass can affect hydrothermal and weathering processes on volcanic edifices (Frank, 1995; Korosec, 1989). The hydrothermal alteration of bedrock can lead to an increased potential for slope failure and resulting lahars (Finn et al., 2001). Additionally, the reduction of glacial mass in the craters can lower overburden pressure and may lead to an increased probability of eruption (Capra, 2008; Tuffen, 2010). Therefore, scenarios of continued climate change leading to ice reduction may increase heat flux to the atmosphere and create a positive feedback loop leading to rapid disintegration of summit ice.

This paper presents unique and first-of-a-kind monitoring data from the fumarole ice caves in the summit craters of Mount Rainier (Frank, 1995; Kiver & Steele, 1975; Zimbleman, 2000). Data collected remotely over the course of 1 year (August 2016–August 2017) include water level, temperature, and specific conductance in an in-cave, melt-associated lake, temperature and pressure of ambient cave air, and the temperature of a nearby active fumarole. These data are compared to the temperature and snowfall accumulation lower on the volcanic edifice as a proxy for summit conditions. Collectively, these data illustrate that, although the fumarole ice caves are persistent features in the summit over many decades, they undergo significant seasonal oscillation, amplified in the firn and modulated at distance from the entrances.

2. Spectral analysis of time-series data

The collection of environmental data on regular intervals over a window of time results in a time-series of information $X(t) = \{X_{t=0}, X_{t=1}, X_{t=2}\ldots, X_{t=N}\}$ from which patterns of behavior of that variable can be elucidated. In the simplest sense, trends or directionality in the value can be linked to processes or external forcing. Similarly, cyclicity in the dataset may reflect the effect of diurnal patterns, synoptic meteorology, or seasonal factors. Comparing multiple time series across the same monitoring window can provide important insight into parallel responses to the same forcing mechanism or causal relationships between independent and dependent variables. Broad-scale analysis of long-term and high-resolution time-series data is a valuable tool for understanding relationships that may otherwise be obfuscated by noise in the data present on shorter time scales.

Correlograms. Autocorrelation and cross-correlation, used to investigate periodicity in data, have been applied across varied disciplines (Mangin, 1984; Peterson et al., 2006; Sokal and Oden, 1978). In autocorrelation, the time-series data are compared with the same data shifted some incremental amount of time—a 'lag.' Correlation coefficients

$$r(k) = \frac{c(k)}{c(0)}, \quad (1)$$

where

$$c(k) = \frac{1}{N}\sum_{i=1}^{N-k}(X_t - \bar{X})(X_{t+k} - \bar{X}), \quad (2)$$

are computed for each lag shift. A plot of the correlation coefficient for every shift provides the auto-correlogram of the data. Auto-correlograms always experience correlation coefficients of unity at 0 lags, and for natural systems, secondary but lower peak correlations or anti-correlations connect to cyclic processes.

In cross-correlation, correlation coefficients are calculated for incremental shifts between two separate time-series data, $X(t) = \{X_{t=0}, X_{t=1}, X_{t=2}\ldots, X_{t=N}\}$ and $Y(t) = \{Y_{t=0}, Y_{t=1}, Y_{t=2}\ldots, Y_{t=N}\}$and a plot of the coefficients

$$r_{XY}(k) = \frac{c_{XY}(k)}{\sigma_X \sigma_Y} \text{ and } r_{YX}(k) = \frac{c_{YX}(k)}{\sigma_X \sigma_Y}, \quad (3)$$

where

$$c_{XY}(k) = \frac{1}{N}\sum_{i=1}^{N-k}(X_t - \bar{X})(Y_{t+k} - \bar{Y}) \text{ and } c_{YX}(k) = \frac{1}{N}\sum_{i=1}^{N-k}(Y_t - \bar{Y})(X_{t+k} - \bar{X}), \quad (4)$$

for each shift produces a cross-correlogram for the two time-series data sets. Peak correlation coefficient in two sets of related variables are never at 0 lags unless the causal nature of the relationship is below the resolution of the sample measurements. The lag number in the correlogram is a measure of the causality, which is the dependent variable and the time structure of that dependency.

Scalograms. Another powerful signal processing tool are wavelets $\psi(t)$, which are functions with zero mean that are localized in time (dt) and frequency ($d\omega$) and satisfy the admissibility condition of Holschneider (1998),

$$C_\psi = \int_{-\infty}^{\infty} \frac{|\hat{\psi}(\omega)|^2}{|\omega|} d\omega < \infty, \quad (5)$$

where $\hat{\psi}(\omega)$ is the Fourier transform of the wavelet function. For a one-dimensional signal of time-series data, the continuous wavelet transform (CWT) can be defined as

$$W_\psi(t,s) = \frac{1}{\sqrt{a}} \int_{-\infty}^{\infty} \psi^* \left(\frac{\tau - t}{s}\right) x(\tau) d\tau \quad (6)$$

where t and s are the analyzing position and the wavelet scale factor, respectively, and ψ^* is the complex conjugate of the wavelet function.

Generalized Morse wavelets are a family of analytic wavelets commonly used because they are suitable for analyzing modulated signals with time-varying amplitude and frequency (Olhede & Walden, 2002) and are standard in mathematical computing software. The Fourier transform of the generalized Morse wavelet is

$$\hat{\psi}_{P,\gamma}(\omega) = U(\omega) a_{P,\gamma} \omega^{\frac{P^2}{\gamma}} e^{-\omega\gamma} \quad (7)$$

where $U(\omega)$ is the unit step, $a_{p,\gamma}$ is a normalizing constant, P^2 is the time-bandwidth product, and γ is a symmetry factor. Plotting the magnitude of the CWT on a graph of frequency versus time produces a scalogram from which regions of greater CWT magnitude reveal patterns that connect to system behaviors.

Cross-wavelet transforms, $W^{XY}=W^X W^{Y*}$, where * represents complex conjugation, the power of that transform $|W^{XY}|$, and the phase of that transform in time-frequency space can explore causal

relationships between two time-series variables (Grinsted et al., 2004). The coherence of that transform, defined by

$$R_t^2(s) = \frac{\left|S(s^{-1}W_t^{XY}(s)\right|^2}{\left(S(s^{-1}|W_t^X(s)|^2\right)\cdot\left(S(s^{-1}|W_t^Y(s)|^2\right)}, \quad (8)$$

with S as a smoothing factor, are effectively correlation coefficients that can be plotted in time-frequency space on a scalogram along with the phase of that relationship.

3. Field location

The volcanic system at Mount Rainier, classified a Decade Volcano by the International Association of Volcanology, is a unique natural laboratory to assess the cycling of glacial melt at the summit crater and on the flanks of the volcanic edifice. Previous research at Rainier and the broader Cascade Volcanic arc (e.g., Frank, 1995; Ingebritsen et al., 2014; Zimbelman, 2000) has provided conceptual models to guide our fundamental understanding of the hydrogeology at Rainier.

The edifice of Rainier formed through successive eruptions of lava and pyroclastic flows over the past 840 ka; the current East and West Craters sit atop a Holocene summit cone nested within the remnants of an older and higher cone that collapsed approximately 5 kabp. Despite recent quiescence, eruptions in the 19th century resulted in extensive (up to 3 x 10^9 m^3) Holocene lahar deposits that blanketed densely populated areas (e.g., Crandell, 1971; Scott et al., 1995). Currently, Rainier is listed as a high risk site in the National Volcanic Early Warning System by the U.S. Geological Survey (Ewert et al., 2005).

The summit of Mount Rainier is a harsh environment. Even at the Paradise Visitors Center, at 1600 m above mean sea level (amsl), the weather includes winter conditions from November through May and is subject to near-continuous sub-zero temperatures starting in December and lasting through March. Snow accumulation picks up in November and reaches a peak depth by March–April; the total snow accumulation at Paradise was 17.9 m in the 2016–2017 season (MORA, 2020).

Thick annual snow accumulation since the last eruption cycle in the 19th century has collected in the twin craters on Rainier, which are filled with plugs of thick glacial ice. Annual snowpack and 25 glaciers blanket the volcanic edifice; the glacial volume is maintained through a delicate balance between climate and volcanic activity. Increasing temperatures (3 C^{o}/ka) and mean freezing levels (220 m/ka), combined with decreasing snowfall (5.1 cm/yr) has contributed to a corresponding 25% reduction in the glacier mass since 1913 and a 14% reduction between 1970 and 2008 (Hoffman et al., 2014; Nylen, 2004; Sisson et al., 2011).

More than 100 slightly acidic fumaroles, driven by hydrothermal cycling of glacial melt along the contact between the summit ice plugs and the crater floor (Frank, 1995), have formed the world's largest fumarole ice cave system in the East Crater. Earlier mapping efforts (Kiver & Steele, 1975; Zimbelman, 2000) were revised and extended during detailed mapping expeditions in 2015–2017. The teams positioned 6,535 individual georeferenced survey shots using DistoX technology with a resulting wire-mesh plot comprising more than 3.5 km of passage that circumnavigates the crater rim and spans a vertical range of 144 m (Figure 1). The highest entrance to the system (4373 m-amsl) is located 19 m below Columbia Crest and is the highest known cave entrance in North America.

The fumarole ice caves and the subglacial lakes in the summit craters are a persistent feature following the development of the glacial plug. In 1855, Indian guide Saluskin noted a crater lake with steam vents following eruptions in earlier decades (*Haines, 1962*). By 1870 an ice plug had developed along with fumarole caves; rocks rolling downslope through these caves splashed in water during summit explorations in 1911 (*Flett, 1912*) and again in 1954 (*Molenaar, 1979*). Lake Muriel was observed in the West Crater in the 1970s, but expeditions from 2014 through 2017 noted that it was not accessible and had likely disappeared. In the East Crater a team encountered Lake Adélie (Figures 1 and 2), unknown to early mapping efforts; in September 2014, Lake Adélie was frozen about 0.7 m thick.

4. Methods and data processing

Primary data for this study were collected during and between summit expeditions in August 2016 and August 2017 from the Climber's Refuge (southern) section of the cave, including Lake Adélie, in the circum-crater passage and fumaroles in the large rooms to the east (Figures 1 and 2). The data comprise passage survey data and field measurements of water quality combined with discrete water samples. Key to this manuscript are monitoring data collected in Lake Adélie every 15 minutes using a calibrated and nonvented In-Situ AquaTroll 200 for specific conductance, temperature, and transducer pressure alongside a paired BaroTroll for air temperature and pressure. Corrections for air pressure in the transducer data yielded water depth in the lake. Three fumaroles were instrumented with GeoPrecision M-Log5W-CABLE temperature sensors for data every 5 minutes and subsampled for hourly averages. Supplementing this study are hourly temperature and snowpack depth SNOWTEL data collected and archived by the U.S. Department of Agriculture, National Resource Conservation Service (NRCS, 2017). Summit temperatures and snow depths are not available; harsh conditions prevent permanent installation and monitoring. As a result, the Paradise data are the best available for comparison. Temperature inversions, cloud cover elevation, and other vertical climate gradients make this comparison tricky.

The incredible story of the datalogger in Lake Adélie was detailed previously by In-Situ (Taylor, 2019). Briefly, the sondes were anchored to a massive boulder (>3 m in each dimension) as all other potential anchor points were unstable (smaller boulders) or mobile (glacial ice). Over the course of the year-long deployment, the massive anchor boulder also proved unstable. At retrieval, the AquaTroll 200 was deeper in the water because of anchor movement and increases to the lake water level, and also wedged between other boulders that slumped into the lake. Remarkably, the sondes stored data for the entire deployment (8/2/2016–8/1/2017); the collective time series plots for all data and includes applied corrections for missing data and instrumentation errors are shown in Figure 3.

What is most striking about the water level data are the apparent rapid changes. The rates of these changes exceed that, explained by increased flux or changes to reservoir shape; small, solitary boulders falling into the lake would not produce the observed increases to water level. Therefore, what is most likely are changes in datum from movements of the anchor boulder;

translational (downslope) motion produces a rapid increase in relative depth as the sonde descends in the water column, and rotational (into the upslope) motion produces a rapid decrease in relative depth as the anchor wire lifts the sonde in the water column. During late April through the end of May 2017, for example, the AquaTroll was entirely out of the water. Therefore, we applied a filter to the data to correct for these changes; thresholds were set to 0.5 mm/hr and 1 mm/hr for translational and rotational motion, respectively, and the instances documented (Figure 3). Given an approximate lake surface area of 200 m^2, these threshold rates translate to approximately 1,700 l/min of recharge and 3,400 l/min of discharge. Decomposing the data, lake level increased by about 2 m (confirmed during the 2017 expedition), and the vertical projection of slope movement was on the order of 2.2 m.

The overlapping patterns and causal relationships in the collected data are also curious. For example, and quite importantly, the first major winter storm in fall 2016 at the end of November produced copious snowfall and a precipitous drop in cave air temperature (Figure 3), especially at Lake Adélie. Interestingly, the temperature of Fumarole 3 (the closest to Lake Adélie) dropped 4 C° during this time, a suite of micro-translational and rotational motions of the anchor block ensued, and the lake surface likely froze over. Following this event, cave temperatures warmed and lake water levels increased significantly in early December 2016 (except December 8–15), initiating another long period of slope instability that lasted until the end of the year.

The observations reported in the previous paragraph necessitated a deeper analysis of the data using signal processing tools in MATLAB. Specifically, the ‘crosscorr,’ ‘cwt,’ and ‘wcoherence’ functions were used to produce auto- and cross-correlograms (Figure 4), CWT scalograms (Figure 5), and wavelet coherence scalograms with phase (Figure 6), respectively. These analyses quantified the timing and magnitude of correlation or anti-correlation across the window of measurement.

5. Results and time series analysis

Water temperatures in Lake Adélie never exceeded 0.5 °C during the study and regularly are at freezing (Figure 3); ice was observed on the lake surface on multiple excursions into the cave

between 2014 and 2017. No vertical temperature gradient was observed in a 2016 survey. The lake water is composed primarily of glacial melt; the single measurements of specific conductance were very low (2.3 µS/cm), the sonde recorded effectively 0 µS/cm during the year of deployment, and the pH is slightly acidic (6.3) with no measured alkalinity. The values of $\delta^{18}O$ and $\delta^{2}H$ are nearly identical to drip waters from cave walls (-19.0 and -132.8‰ versus -18.9 and -131.5‰). It appears, at present, that no hot springs or other thermal upwellings contribute to the lake.

The cave air near Lake Adélie is similarly cold, ranging between -1.0 and 3.0 °C during most of the study with storm systems plunging the cave temperatures to as low as -7.0 °C; observations during this study reveal that the lake area was often the coldest spot of the cave system. The linkage between cave air temperature and lake water temperature is robust with correlation coefficients approaching 0.5 centered on no spectral shift, low-amplitude seasonal-scale correlations and anti-correlations between 1500 and 2500 lags (62 to 104 days), and synoptic-scale alignments of approximately 200 lags (8 days) that are also visible in the auto-correlogram of the cave temperature data (Figure 4). The overall correlation between the cave air temperature and the outside temperature is considerably less, given the known restrictions, with coefficients never less than -0.1 or greater than 0.1, despite considerable longitudinal airflow in the cave passage at Lake Adélie. This airflow was observed as largely clockwise in the cave system during the expedition, with a complex inflow-outflow relationship among the entrances.

In contrast to the cave air temperature, the outside temperature and cave air pressure are observably similar (Figure 3), with correlogram coefficients ranging between -0.3 and 0.4 (Figure 4). No outside pressure readings are available for comparison; however, it is likely that outside and cave pressure are highly correlated except that the cave is sealed by deep snowfall and therefore isolated from the outside environment. Changes in cave air pressure precede those of the outside air with peak cross-correlation lags between 0 and 1500 (0 to 62 days), with short lag times indicating rapid responses to storm events. The wavelet coherence scalogram between cave air pressure and outside temperature (Figure 6A) shows this correlation at timescales of 16 hours, ¾-cycle out of phase, focused more intensely at the beginnings and endings of the monitoring window (summer). The winter months feature response times that are more rapid (<8

hours) and others on the order of 3 days that are largely in phase. Even longer lag times on the correlogram are likely related to a more rapid onset of winter at the summit crater (4000 m) compared to the Paradise Visitors Center (1600 m). Similarly, the anti-correlation peak at -2500 lags (104 days) indicates the arrival of spring temperatures at Paradise 3 months before the summit. These seasonal changes are visible as twin negatively sloped, and in phase peaks of wavelet coherence on the scalogram (Figure 6A), spanning 42-days to 83-days of lag time. The first of these peaks begins in October and the second peak concludes in May.

The cave air temperature at Lake Adélie is not strongly correlated to the cave air pressure, coefficients are never less than -0.15 or greater than 0.2 (Figure 4). Rapid drops in cave air pressures precede increased cave air temperatures on short (weekly) timescales. On the other hand, the drop in cave pressure leads to a weak drop in cave air temperature with a delay of 1800 to 2200 lags (75 to 92 days). This discrepancy may be explained in the correlograms between the cave air pressure and the fumarole temperatures, which have greater coefficients (-0.8 to 0.4 for Fumarole 2; -0.8 to 0.5 for Fumarole 3, and -0.4 to 0.4 for Fumarole 4). At Fumarole 2 there is a visible out-of-phase correlation in the time series data (Figure 4), which is visible in the wavelet coherence scalogram as peak magnitudes across the monitoring window that are centered on a lag of 173 days (Figure 6B). Other strong wavelet coherence occurs at higher frequencies, such as between 3 and 10 days (also out of phase), and timeframes of less than 1 day that are out of phase by one-quarter of a cycle.

That out-of-phase correlation is present but not visible nor as coincident in the correlogram between the cave air pressure and the temperature of Fumarole 3 (Figure 4); however, the wavelet coherence scalogram shows this clear correlation in a time frame of approximately 140 days having the same higher frequency correlations and phase relationships as at Fumarole 2 (Figure 4). In contrast for Fumarole 4, changes to cave air pressure precede an anti-correlated change in fumarole temperature by approximately 1500 lags (62 days). The wavelet coherence scalogram is less clear but clearly shows the same higher-frequency correlations and phase relationships as at Fumaroles 2 and 3 (Figure 6B and 6C).

All three fumaroles monitored in this study have very different temperature profiles and trajectories, despite the observed correlations with cave air pressure (Figure 3). At Fumarole 2, the CWT scalogram (Figure 5) reveals that changes spanning 4 to 20 days are most impactful in the first 100 days of the monitoring before the onset of winter. Shorter duration (<3 day) events are more frequent in the middle and end of the monitoring study. At Fumarole 3, the CWT scalogram shows the similar timing and magnitude of these shorter duration events; however, synoptic-scale changes are more prevalent across the study duration and a long-term event exceeding 90 days in duration. The CWT scalogram of the temperature data from Fumarole 4 is less governed by the shorter-duration events and broadly defined by events spanning 10 days and 20 to 25 days in the first half of the study.

Correlation coefficients between the temperature of each fumarole and the cave air temperature are weak (-0.15 to 0.15 for Fumarole 2; -0.15 to 0.1 for Fumarole 3, and -0.25 to 0.2 for Fumarole 4) but have strong cyclicity in the representative correlograms (Figure 4). At Fumarole 2, there is a convex parabolic temperature profile having peak temperatures of 55 °C in March 2017; the correlogram has positive correlation at 0 lags and oscillates between correlation and anti-correlation approximately every 2000 lags (83 days). The same oscillation is true but more diminished in the correlogram for Fumarole 3; however, the time series is dominated by a strong downward trend in temperature (from 51 to 41 °C) starting with a precipitous drop in November 2016. At Fumarole 4, where average temperatures remain above 55 °C, the oscillations in correlation with cave air temperature every 62 days are present, but are in reverse phase to the other two fumaroles.

Of particular importance are the strong apparent correlations between most variables and the depth of snow at the Paradise Visitors Center (Figure 3). These correlations have expected lag shifts in phase when compared with the outside temperature having coefficients of 0.4 at -1500 lags (62 days) and -0.3 at 2000 lags (83 days), and the cave air pressure with coefficients of 0.5 at -2200 lags (92 days) and -0.5 at 1000 lags (42 days); peak snow depth is shifted from peak winter temperatures and pressures (Figure 4). This same lag and out-of-phase relationship is visible on the wavelet coherence scalogram in the timeframe from September 2016 through March 2017 (Figure 6E). A similar, but less clear correlogram results when comparing the

temperature of Fumarole 4 to the snow depth with coefficients of 0.3 at -1500 lags (62 days) and a dual minimum of -0.2 centered on 2000 lags (83 days). Fumaroles 2 and 3 have a reverse but strong correlations with snow depth; the correlogram with Fumarole 2 has coefficients of -0.5 at -2500 lags (104 days) and 0.7 centered on 1000 lags (42 days), and Fumarole 3 has coefficients of -0.8 at -1200 lags (50 days) and 0.5 centered on 4000 lags (167 days). This same lag shift in phase propagates to the correlogram between the pressure transducer reading from Lake Adélie and the snow depth having coefficients of -0.5 at -400 lags (17 days) and 0.4 at 1800 lags (75 days).

6. Discussion

The dynamics of climate and heat flux on active volcanic edifices with a glacial mantle are the major influence on fumarole activity, and thus, the size and morphology of fumarole caves. To date, exploration and study of similar fumarole ice cave environments in nearby Mount Saint Helens (Curtis, 2020) and Mount Erebus in Antarctica (Wardell et al., 2003) have not produced similar data that monitor the fumarole cave environment that is inaccessible during much of the year; distributed fiber optic temperature sensing at Mount Erebus spanned a period of only 1 week (Curtis & Kyle, 2011). At Mount Saint Helens, observations in recent expeditions indicate that similar patterns exist (C. Stenner, personal communication, 2020).

Our original goal was to determine if fluctuations in heat flux and volcanic gas translate into changes in water level from melt and water chemistry from dissolved gas. Given the available data, these volcanic gas events did not occur; the specific conductivity remained 0 μS/cm during the entire measurement period and was therefore not used in our time-series analysis. This is consistent with gas concentration observations during each expedition, monitored as a condition of exploration. Only Fumarole 4, the hottest of the three monitored, largely unaffected by changes to the outside and cave climate, and on the north rim of the crater near Columbia Crest (Figure 1), reported significant CO_2 and detectable SO_2 and H_2S. Fumaroles 2 and 3 are primarily of recycled atmosphere and steam; we observed only traces of CO_2. The East Crater was the site of most recent volcanism and is cooler and more quiescent; the focus of heat flux and volcanic

gas emissions appears to have shifted toward the West Crater where fumarole temperatures remain consistently higher than elsewhere.

In contrast to the water chemistry, the measured position of the pressure transducer in Lake Adélie fluctuated considerably and reported a significant increase in depth over the measurement window—the sonde moved and the lake water level rose. Given no detectable change in volcanic activity, the observations must connect the fumarole cave microclimate on Mount Rainier to external climate forcing.

Using the measured cave air pressure as a proxy, the onset of frigid temperatures and snowpack arrives earlier (October) and ends later (May) above 4000 m-amsl (Figure 3). The depth of the summit snowpack was not measured and not available, but is probably greater than the total accumulation than at lower elevations. Inside the cave, an ice screw used as an anchor moved downward almost 8 m during the year between the 2016 and 2017 campaigns. Using an average density of 800 $kg \cdot m^{-3}$ for the glacial ice and assuming a snow density of 100 $kg \cdot m^{-3}$, this translates to a summit snow accumulation of 64 m, not accounting for significant ablation.

The cave air pressure is a better proxy for external climate than the cave air temperature because the glacial ice and fumarole output buffers rapid changes. Even with this, storm systems bring about major short-term changes to the air temperature and pressure in the cave; air pressure equilibration occurs rapidly (within 16 hours in the summer months and less than 8 hours in the winter). Frigid temperatures in the cave lead to a response in lake water temperature over the period of a week, with thick surface ice developing during extended periods of subzero temperatures.

Changes to cave air pressure exerts some influence on fumarole temperature. This is most clearly seen at Fumarole 2 where the annual cycle of cave air pressure generates an opposite change in fumarole temperature. At Fumarole 3, the closest to Lake Adélie, this same trend is present at the beginning of the monitoring period but is truncated by a major drop in temperature. That drop occurs in concert with other changes happening in summit environment. To explore those

changes, we considered the two following windows of time associated with winter storm systems: November 27–December 31, 2016 and February 2–February 21, 2017.

By November 27, 2016, several days of snowfall at elevation contributed to the first major increase of snowpack on the mountain. Temperatures and pressures subsequently plummeted that day, propagating into the cave and further cooling lake water temperatures. The temperature of Fumarole 2 was already falling by that time and continued to drop through November 29. After a cave-air temperature minimum of -5.0 °C on November 28, the cave air temperature and pressure sharply increased though December 2 for the pressure and December 6 for the temperature, at which point the lake water temperature climbed above freezing. The depth of the pressure transducer fluctuated significantly in this window, falling and rising as a result of a series of translational and rotational motions of the anchor block. Water levels continued to rise through December 15, likely through increased melt. In the last half of December, anchor block motion occurred regularly.

On February 2, 2017, a major storm system significantly increased snow depths through February 6. Twin cold air pulses permeated the cave on February 6 and 11 with continuous low cave air pressure readings. The lake temperature reached freezing. The anchor block, which had been stable for several days, moved and rotated many times between February 4 and 11, when it slowed down its motion after cold air pulses ended. The temperature of Fumarole 3 experienced a short increase prior to February 6 and then dropped by almost 4.0 C° by February 13 and remained depressed. After the cold air pulse on February 11 ended and the cave air pressure spiked on February 12, cave air and lake temperatures steadily increased through February 21. Water level rise accelerated through February 19, likely through increased melt, and then the anchor block rotated, shifting the measurement datum of the pressure transducer upward by 20 cm.

Generalizing these two events to a pattern and supported by the time-series analyses, the following sequence appears to govern major changes to the cave microclimate and lake levels (Figure 7). Major winter storms move through the region, bringing heavy snowfall and causing outside temperatures to plunge. Cave temperatures similarly plunge rapidly, which cause Lake

Adélie (and the adjacent saturated talus slopes) to freeze. The heavy snowfall seals the cave entrances along the crater rim, and cave air pressure rises from continued fumarole output. Cave air temperatures begin to rise again, causing the lake surface and adjacent saturated slopes to thaw. The rapid melt and trapped fumarole steam accumulate in Lake Adélie and cause rising lake levels. Melting proceeds and reopens the cave entrances. Repeating freeze-thaw cycles cause mass wasting (slope creep, slump, and rock fall) on the sloped floor of the cave passage, which translate to rapid changes in lake level owing to the shifting position of the piezometer. Over the course of our year-long monitoring, lake level rose approximately 2 m and the vertical projection of the datum shifted downward in the water column by an additional 2.2 m (Figure 3).

The cycle speaks to the persistently cold but surprisingly dynamic physical environment of the Rainier fumarole caves. Despite these seasonal variations, the dynamic equilibrium between thermal flux, glacial movement, mass wasting, and recycling of meltwater via fumarole steam is what maintains the scale and morphology of these caves on decadal or longer scales. Certainly, changes to any one of the above variables introduces an imbalance. Reductions in glacier mass over the past several decades have visibly altered the mountain, but the fumarole ice caves seem largely stable at depth; the number and size of passages and entrances in the firn near the crater rim is different. This equilibrium is not the case with the explored fumarole caves in the caldera of nearby Mount Saint Helens, where cycles of glacial ice accumulation and ablation are tied to dramatic changes in heat flux and periods of volcanism (Sobolewski et al., 2020).

The detailed temperature measurements of fumarole temperature show that interannual changes are occurring on the Rainier summit. What is not known is the extent to which these changes represent changes in heat flux. This is because two very important datasets are missing. The first is the measurements of fumarole output. Some attempts were made at measuring gas flow at key fumaroles, but those measurements occurred only during expeditions and were of limited resolution. The second missing dataset is air flow measurement in the cave, which is known from expeditions to be significant. Attempts were made in 2017 to install ultrasound anemometers to collect wind velocity at three key locations near Fumaroles 2, 3, and 4. Unfortunately, equipment and battery problems prevented data collection except for a diurnal cycle at each location.

The cause for changes to fumarole temperatures are not adequately known, but our results do show a connection to seasonal and shorter changes to the cave microclimate. Fumarole 4 is the hottest, closest to the current thermal center near Columbia Crest, and takes a longer time to respond to climate forcing. Fumaroles 2 and 3 also have elements of these synoptic-scale and longer responses, but respond to some climate events, particularly winter storms, in a few days. This is likely because Fumaroles 2 and 3 are largely composed of recycled atmosphere and not volcanic gas, supported by gas measurements in our expeditions and the geochemistry presented in Zimbelman et al. (2020). The longer-term trends in temperature observed in Fumaroles 2 and 3 are quite interesting. The annual cycle in Fumarole 2 and its anti-correlation to cave air pressure may be explained by a process where lower pressures in the winter generate a vacuum to enhance the flux of gas and therefore heat. The long-term drop in temperature at Fumarole 3 is more complicated. At some level, the trend may be from an overall change in the locus of heat flux toward Columbia Crest and the West Crater. It is also possible that increased melt and corresponding higher lake levels increase recharge at the base of the glacial plug. If this were so, amplified production of steam in that part of the upper edifice could both cool the heat source and increase the fumarole volume.

7. Conclusions

Ice dynamics in the summit glacier of Mount Rainier is a modulator of fumarole activity. In the year of hourly monitoring data presented in this paper, variations are clearly observed in cave air temperature and pressure, fumarole temperature, and water level in a melt-formed lake; these variations are related to synoptic- to seasonal-scale meteorological patterns. Spatial and temporal patterns within the cave are likely connected to variations in volcanic heat flux and the circulation of glacial melt. During the winter season, major snowfall seals the cave entrances, creating a positive feedback loop until entrances reopen from rising cave air temperature and pressure from fumarole output leads to elevated lake levels from increased melt. Observed freeze-thaw cycles in the cave lead to crater mass wasting. The morphology of the fumarole ice cave is maintained on decadal or longer scales by fumarole gas convection and advection, representing a dynamic equilibrium between thermal flux, glacial movement, mass wasting, and recycling of meltwater via fumarole steam. While the fumarole ice caves seem largely stable in

the present configuration, long-term trends in climate and ice volume at Mount Rainier have visibly altered the mountain and may disrupt the dynamic equilibrium of these caves, alter the rate of mass wasting and fluid circulation, and change the long-term prognosis for active volcanism.

8. Acknowledgments

Research approved by research, climbing, and wilderness permits issued by the National Park Service. Direct expedition funding was provided by the following grants to Glacier Cave Explorers and managed by E. Cartaya: National Geographic Expeditions Council, Mazamas Research Grant, Mountain Rescue Association, Petzl, and REI. Key corporate sponsorships provided expedition equipment, food, and supplies. Industrial Scientific provided portable gas monitors for the expedition. Special Projects Operations supplied SCBA equipment for exploration. Cracker Jack First Response Specialists of Bend, OR, facilitated logistics for the 2015 field expedition. More than 100 people facilitated these studies by hauling scientific and expedition equipment to the summit and back.

References

Bertozzi, B., Pulvirenti, B., Colucci, R. R., & Di Sabatino, S. (2019). On the interactions between airflow and ice melting in ice caves: A novel methodology based on computational fluid dynamics modeling. *The Science of the Total Environment, 669*, 322–332. doi:10.1016/j.scitotenv.2019.03.074

Capra, L. (2008). Abrupt climatic changes as triggering mechanisms of massive volcanic collapses. *Journal of Volcanology and Geothermal Research*, *155*, 329–333. doi:10.1016/j.jvolgeores.2006.04.009

Crandell, D.R. (1971). Postglacial lahars from Mount Rainier volcano, Washington: *U.S. Geological Survey Professional Paper 667*, 75 p.

Curtis, A., & Kyle, P. (2011). Geothermal point sources identified in a fumarolic ice cave on Erebus volcano, Antarctica using fiber optic distributed temperature sensing. *Geophysical Research Letters, 38*(16). doi: 10.1029/2011GL048272

Curtis, A.G. (2020). Comparison of Earth's fumarolic ice caves, with implications for icy voids on other worlds. Paper presented at 3rd International Planetary Caves Conference, San Antonio, Texas. LPI Contribution No. 2197, id.1070.

Edwards, B.R., Gudmundsson, M.T., & Russell, J.K. (2015). Glaciovolcanism. In H. Sigurdsson, B. Houghton, H. Rymer, J. Stix, & S. McNutt (Eds.), *The Encyclopedia of Volcanoes*. Academic Press, pp. 377–393

Ewert, J.W., Guffanti, M., & Murray, T.L. (2005). An assessment of volcanic threat and monitoring capabilities in the United States: Framework for a National Volcano Early Warning System. *U.S. Geological Survey Open File Report 2005-1164*.

Finn, C.A., Sisson, T.W., & Deszcz-Pan, M. (2001). Aerogeophysical measurements of collapse-prone hydrothermally altered zones at Mount Rainier volcano. *Nature, 409*, 600–603. doi:10.1038/35054533

Flett, J.B. (1912). The thermal caves. *The Mountaineer*, 5, 58–60.

Frank, D. (1995). Surficial extent and conceptual model of hydrothermal system at Mount Rainier. *Journal of Volcanology and Geothermal Research, 65*, 51–80.

Giggenbach, W.F. (1976). Geothermal ice caves on Mt Erebus, Ross Island, Antarctica *New Zealand Journal of Geology and Geophysics* 19(3): 365– 372.

Grinsted, A., Moore, J. C., & Jevrejeva, S. (2004). Application of the cross wavelet transform and wavelet coherence to geophysical time series. *Nonlinear Processes in Geophysics., 11*, 561–566. https://doi.org/10.5194/npg-11-561-2004, 2004

Gulley, J. D., Benn, D. I., Screaton, E., & Martin, J. (2009). Mechanisms of englacial conduit formation and their implications for subglacial recharge. *Quaternary Science Reviews, 28*(19-20): 1984-1999.

Haines, A.L. (1962). *Mountain fever, historic conquests of Rainier*: Portland, OR, Oregon Historical Society, 278 p.

Hoffman, Jr., R., Woodward, A., Haggerty, P., Jenkins, K.J., Griffin, P.C., Adams, M.J., et al. (2014). Mount Rainier National Park - Natural resource condition assessment. *National Park Service Natural Resource Report NPS/MORA/NRR-2014/894*, 380 p.

Holschneider, M. (1998). *Wavelets: An analysis tool*. Oxford: Oxford University Press.

Ingebritsen, S.E., Randolph-Flagg, N.G., Gelwick, K.D., Lundstrom, E.A., Crankshaw, I.M., Murveit, A.M., et al. (2014). Hydrothermal monitoring in a quiescent volcanic arc: Cascade Range, northwestern United States. *Geofluids, 14*, 326–346. doi: 10.1111/gfl.12079

Kiver, E.P., & Steele, W.K. (1975). Firn caves in the volcanic craters of Mt Rainier, Washington. *National Speleological Society Bulletin, 37*(3), 45–55.

Korosec, M.A. (1989). Geothermal resource evaluation of Mount Rainier. U.S. Department of Interior, Bureau of Land Management, Lacey, WA, p. 61.

Luetscher, M., & Jeannin, P.-Y. (2004). The role of winter air circulations for the presence of subsurface ice accumulations: An example from Monlési ice cave (Switzerland). *Theoretical and Applied Karstology, 17*, 19–25.

Mangin, A. (1984). Pour une meilleure connaissance des systèmes hydrologiques à partir des analyses corrélatoire et spectrale. *Journal of Hydrology 67*, 25–43. doi.10.1016/0022-1694(84)90230-0

Meyer, C., Meyer, U., Pflitsch, A., & Maggi, V. (2016). Analyzing airflow in static ice caves by using the calcFLOW method. *The Cryosphere, 10*: 879–894. doi:10.5194/tc-10-879-2016

Molenaar, D. (1979). *The Challenge of Rainier: A Record of the Explorations and Ascents, Triumphs and Tragedies, on the Northwest's Greatest Mountain*: Seattle, WA, Mountaineers Books, 384 p.

MORA (2020). https://www.nps.gov/mora/planyourvisit/annual-snowfall-totals.htm, accessed on May 25, 2020.

NRCS (2017). https://www.nrcs.usda.gov/wps/portal/nrcs/detail/or/snow/, accessed August 15, 2017.

Nylen, T.H. (2004). Spatial and temporal variations of glaciers (1913-1994) on Mount Rainier and the relation with climate (Master's thesis). Portland, OR: Portland State University.

Ohata, T., Furukawa, T., & Higuchi, K. (1994). Glacioclimatological study of perennial ice in the Fuji ice cave, Japan. Part 1. Seasonal variation and mechanism of maintenance. *Arctic and Alpine Research 26*(3), 227-237.

Olhede, S.C., & Walden, A.T. (2002). Generalized Morse wavelets. *IEEE Transactions on Signal Processing*, 50(11), 2661–2670.

Persoiu, A., & Lauritzen, S.E. (Eds.). (2017). *Ice Caves*. Elsevier.

Peterson, E.E., Merton, A.A., Theobald, D.M., & Urquhart, N.S. (2006). Patterns of spatial autocorrelation in stream water chemistry. *Environmental Monitoring and Assessment 121*(1-3), 571–596.

Pflitsch, A., Cartaya, E., Mc Gregor, B., Holmgren, D. and B. Steinhöfel (2017). Climatologic studies inside Sandy Glacier at Mt. Hood Volcano in Oregon. *Journal of Cave & Karst Studies*, Vol. 79 (3), S. 189 – 206, doi: 10.4311/2015IC0135

Scott, K.M., Vallance, J.W., & Pringle, P.T. (1995). Sedimentology, behavior, and hazards of debris flows at Mount Rainier, Washington: *U.S. Geological Survey Professional Paper 1547*, 56 p.

Sisson, T.W., Robinson, J.E., & Swinney, D.D. (2011). Whole-edifice ice volume change A.D. 1970 to 2007/2008 at Mount Rainier, Washington, based on LiDAR surveying. *Geology*, 39(7), 639-642. doi: 10.1130/G31902.1

Sobolewski, L. Pflitsch, A. Stenner, C., 2020. Studies inside Newly Formed Glacier & Firn Caves in the Crater of Mount Saint Helens (Washington, USA), Poster at: Physics of Volcanoes, Hamburg, Feb. 2020.

Sokal, R.R., & Oden, N.L. (1978). Spatial autocorrelation in biology: 1. Methodology. *Biological Journal of the Linnean Society 10*(2), 199-228.

Taylor, H. (2019). Science Explorers Battle Elements to Study the Inner Workings of Glacier Caves, https://in-situ.com/us/blog/science-explorers-battle-elements-research-inner-workings-glacier-caves/, accessed June 18, 2020.

Tuffen, H., Pinkerton, H., McGarvie, D.W., & Gilbert, J.S. (2002). Melting of the glacier base during a small-volume subglacial rhyolite eruption: Evidence from Bláhnúkur, Iceland. *Sedimentary Geology 149*(1-3), 183–198.

Tuffen, H. (2010) How will melting of ice affect volcanic hazards in the twenty-first century?: *Philosophical Transactions of Royal Society A, 368*, 2535–2558. doi:10.1098/rsta.2010.0063

Wardell, L.J., Kyle, P.R., & Campbell, A.R. (2003). Carbon dioxide emissions from fumarolic ice towers, Mount Erebus volcano, Antarctica. In C. Oppenheimer, D.M. Pyle, & J. Barclay (Eds.), Volcanic Degassing. *Special Publication of the Geological Society 213*, p. 231–246.

Williams, K.E., & McKay, C. (2015). Comparing flow-through and static ice cave models for Shoshone Ice Cave. *International Journal of Speleology*, *44*(2), 1.

Zimbelman, D.R., Rye, R.O., & Landis, G.P. (2000). Fumaroles in ice caves on the summit of Mt Rainier–Preliminary stable isotope, gas, and geochemical studies: *Journal of Volcanology and Geothermal Research*, *97*, 457–473.

Figure Captions

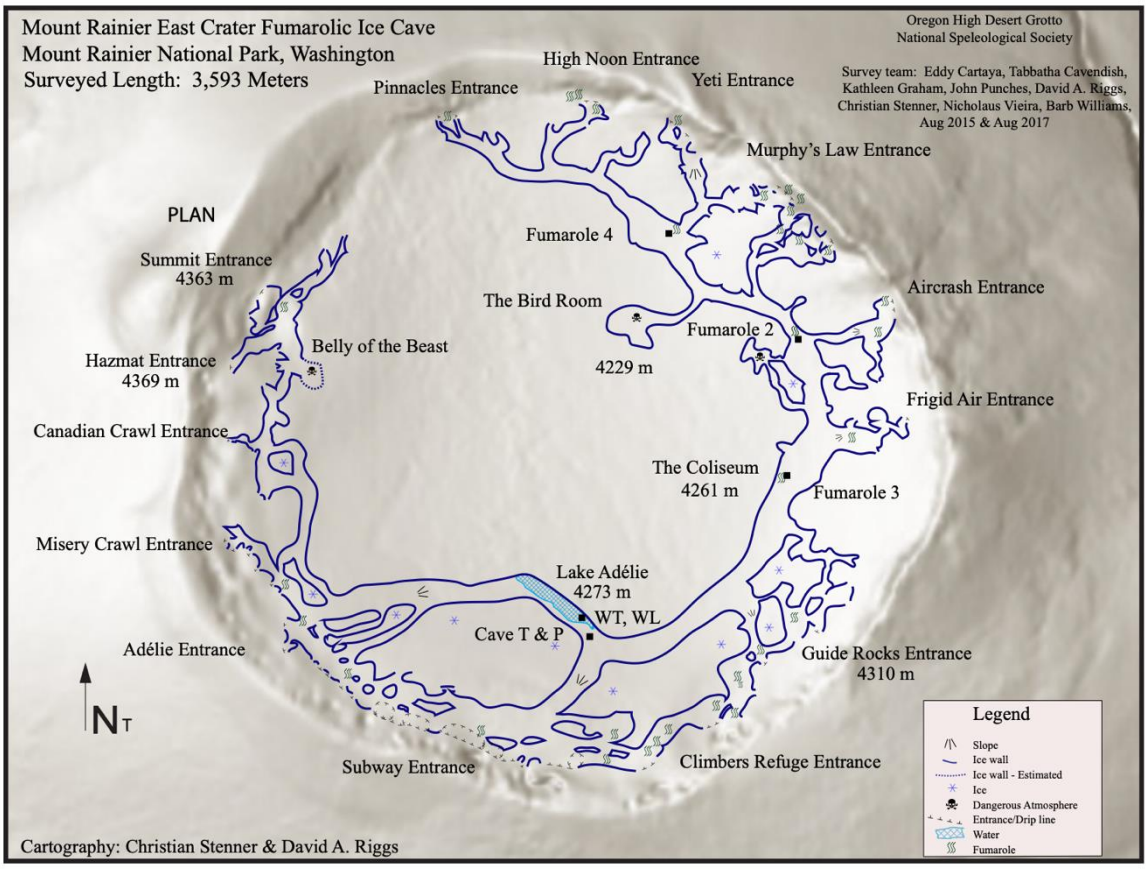

Figure 1. Map of fumarole ice caves in the East Crater of the summit of Mount Rainier. Map legend lists a key to features. Base map is a shaded digital elevation model of elevation. Monitoring locations shown for fumarole temperature, cave-air temperature and pressure, and lake temperature and depth. Outside temperature and snow depth measurements are from the Paradise Visitors Center (not visible on this map).

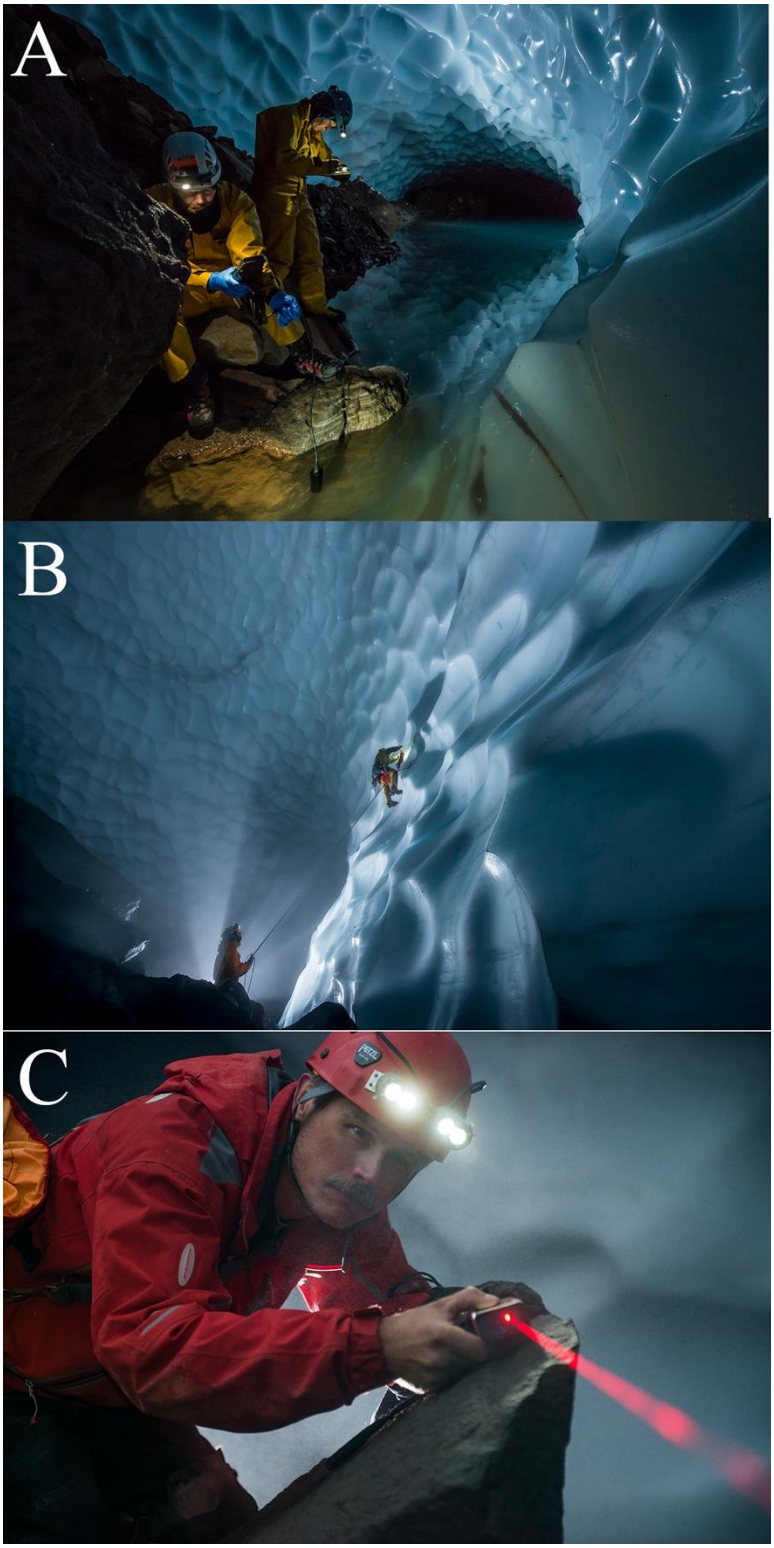

Figure 2. Photos from inside the fumarole ice caves in the East Crater summit of Mount Rainier. A) Lake Adélie during water sampling in 2015. B) Ice climber in the Colosseum Room (Figure 1) installs an ice screw for ice ablation and movement measurements in 2015. C) Expedition member conducts laser range-survey of passage dimensions in 2015. Photos courtesy of Francois-Xavier De Ruydts.

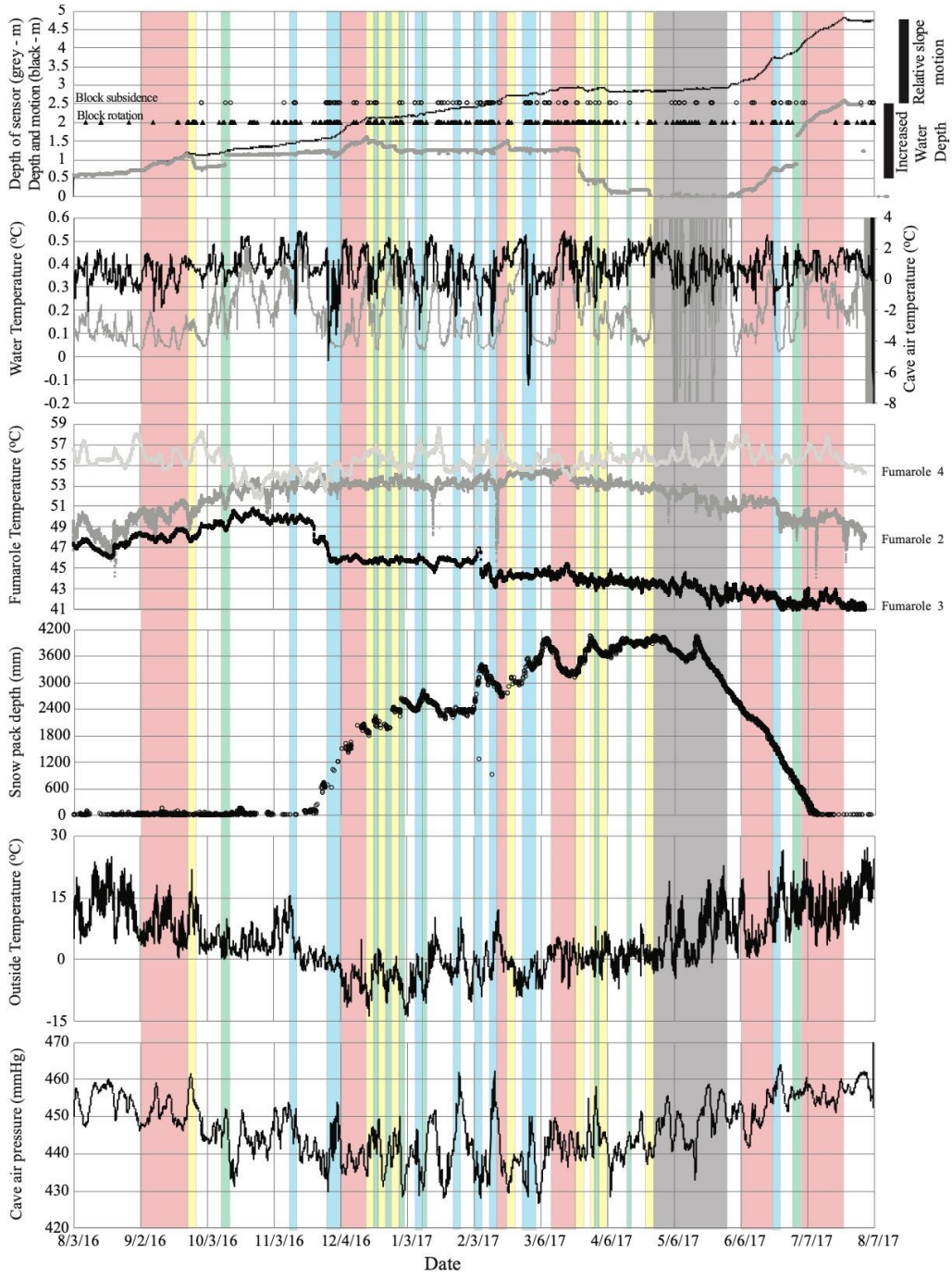

Figure 3. Accumulated hourly time series data from sondes at Lake Adélie, in fumaroles, and at the Paradise Visitors Center. Piezometer measurements at Lake Adélie have been corrected to original datum and instances of anchor boulder motion (translational and rotational) are identified. Periods of time when the surface of Lake Adélie is frozen are shown as blue bars. Periods of rapid increases in water level due to enhanced melt are indicated by red bars. Periods of key translational and rotational motion of anchor boulder are shown as green and yellow bars, respectively. The period of time the peizometer is out of water is shown as gray bar.

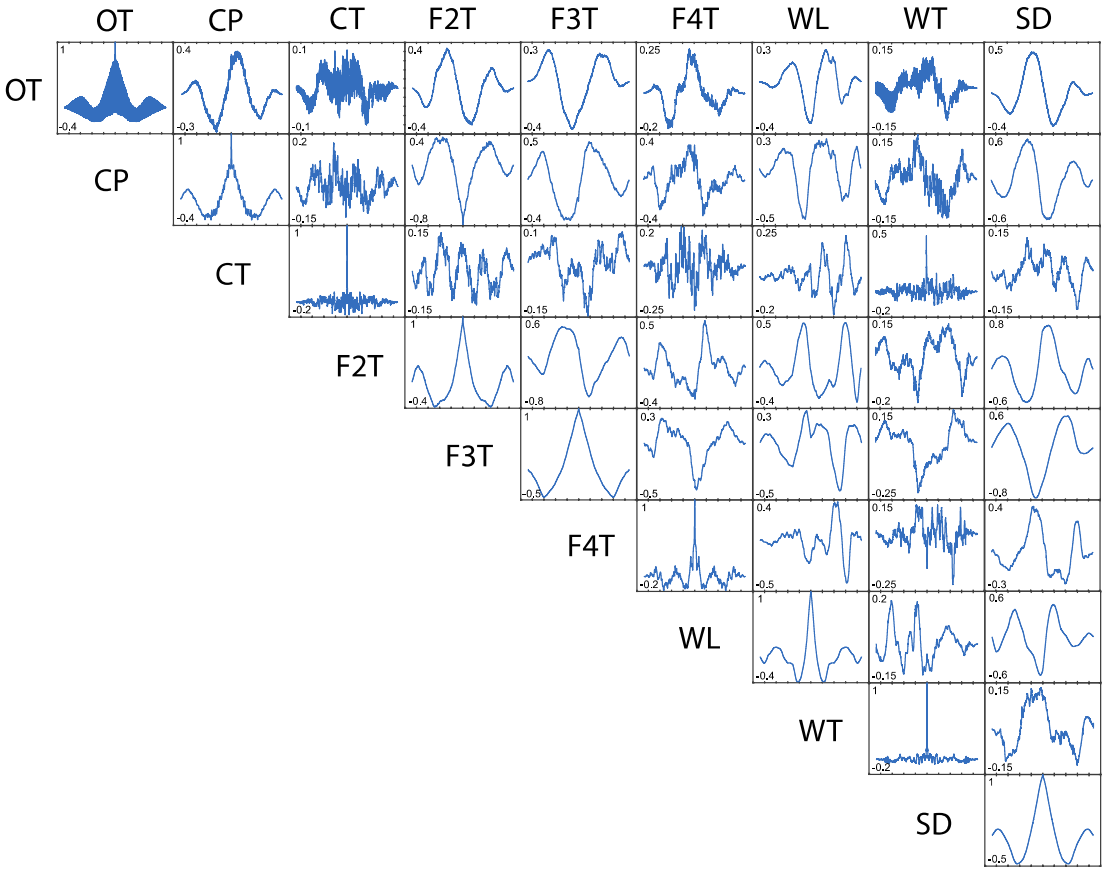

Figure 4. Matrix of auto- and cross-correlograms produced in using the 'crosscorr' function in MATLAB. Auto-correlograms are aligned on the diagonal. Upper and lower bounds of correlation coefficients are indicated for each correlogram. Horizontal ticks on correlograms are in increments of 2,000 lags (83.3 days). OT – outside temperature at Paradise Visitors Center, CP – cave pressure, CT – cave temperature, F2T – fumarole 2 temperature, F3T – fumarole 3 temperature, F4T – fumarole 4 temperature, WL – Lake Adélie water level, WT – Lake Adélie water temperature, SD – snow depth at Paradise Visitors Center.

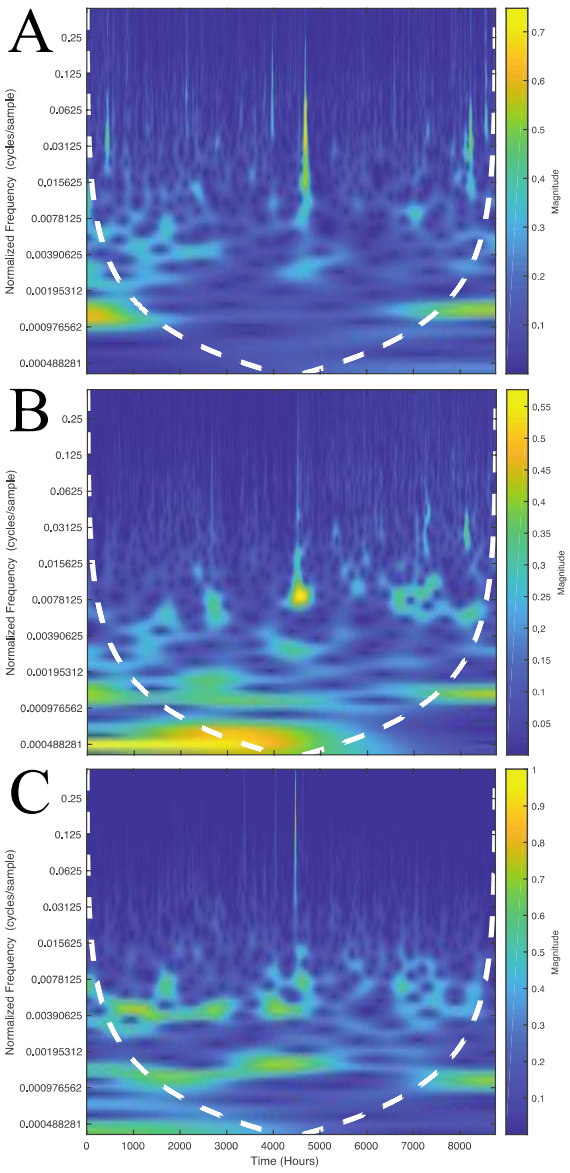

Figure 5. (CWT) scalograms of fumarole temperatures produced in MATLAB—A) Fumarole 2, B) Fumarole 3 and C) Fumarole 4. The scalogram is the absolute value of the CWT plotted as a function of time and frequency with correlation magnitude shown for each scalogram. Frequency is plotted on a logarithmic scale. The cone of influence showing where edge effects become significant is indicated by a white dashed line.

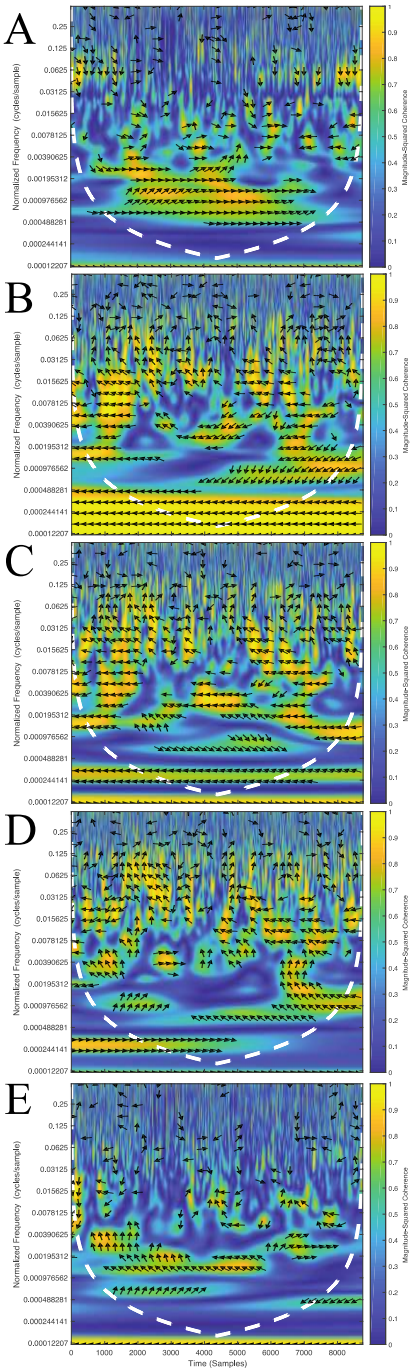

Figure 6. Wavelet coherence scalograms produced in MATLAB with phase shown as black arrows (horizontal-right orientation indicates in-phase alignments; a one-half counter-clockwise rotation is an out-of-phase alignment)—A) cave air pressure and outside temperature at the Paradise Visitors Center, B) cave air pressure and Fumarole 2 temperature, C) cave air pressure and Fumarole 3 temperature, D) cave air pressure and Fumarole 4 temperature, E) snow depth at Paradise Visitors Center and the cave temperatures. The scalogram is the absolute value of the coherence plotted as a function of time and frequency with correlation magnitude shown for each scalogram. Frequency is plotted on a logarithmic scale. The cone of influence showing where edge effects become significant is indicated by a white dashed line.

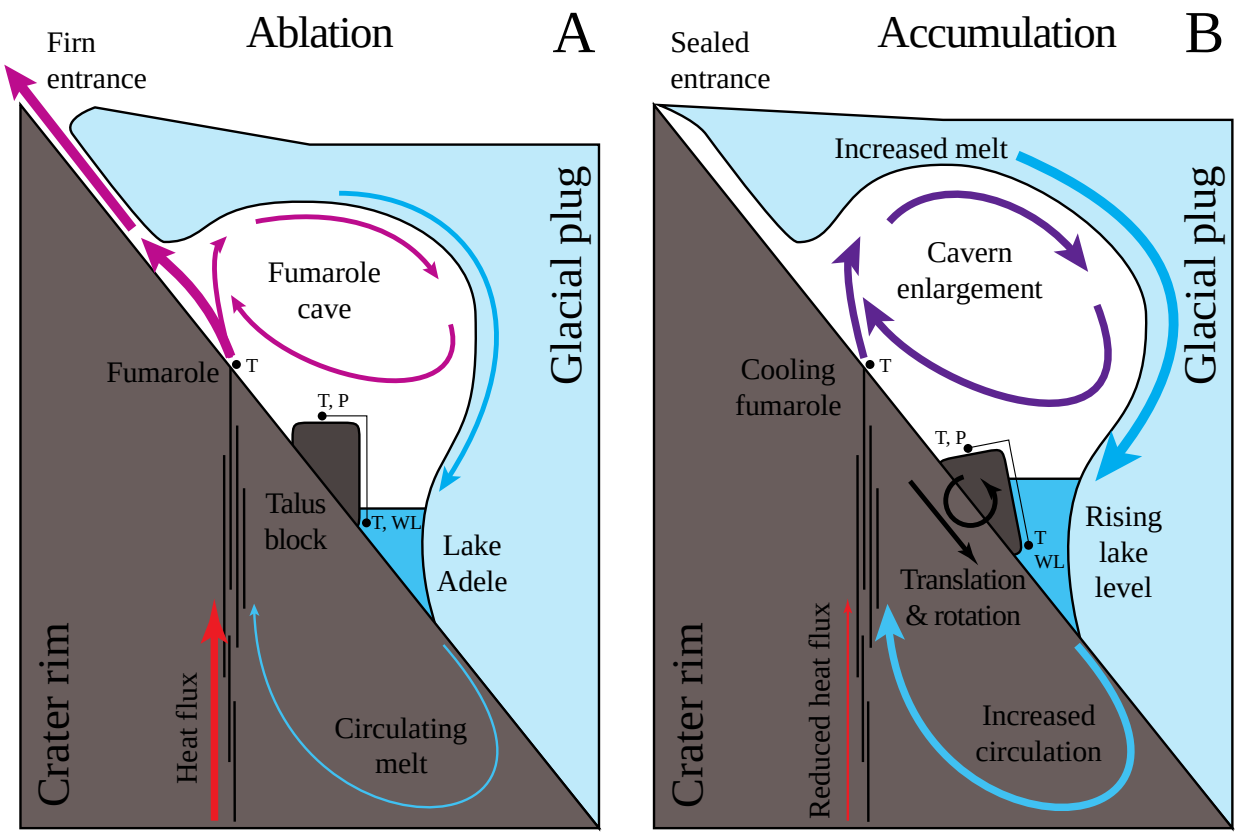

Figure 7. Schematic of processes within fumarole caves on Mount Rainer during periods of A) ablation during summer months where the caves are open to the outside environment, and B) during periods of accumulation during the winter months when the caves are often sealed from the outside environment from increased snowpack.

Figure 1.

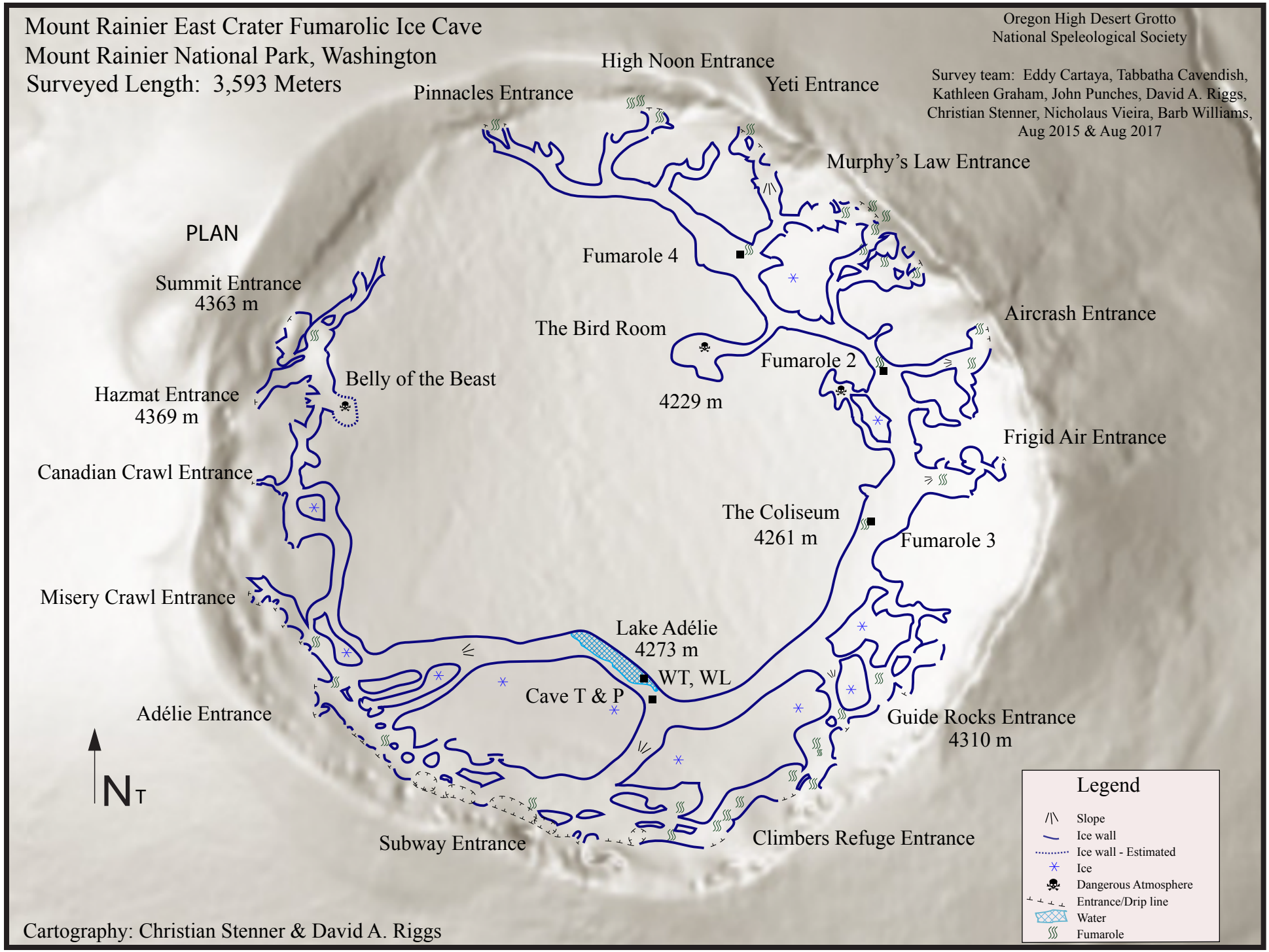
Mount Rainier East Crater Fumarolic Ice Cave
Mount Rainier National Park, Washington
Surveyed Length: 3,593 Meters
Oregon High Desert Grotto
National Speleological Society
Survey team: Eddy Cartaya, Tabbatha Cavendish, Kathleen Graham, John Punches, David A. Riggs, Christian Stenner, Nicholaus Vieira, Barb Williams, Aug 2015 & Aug 2017
PLAN
High Noon Entrance
Pinnacles Entrance
Yeti Entrance
Murphy's Law Entrance
Fumarole 4
Summit Entrance
4363 m
The Bird Room
Aircrash Entrance
Fumarole 2
Belly of the Beast
Hazmat Entrance
4369 m
4229 m
Frigid Air Entrance
Canadian Crawl Entrance
The Coliseum
4261 m
Fumarole 3
Misery Crawl Entrance
Lake Adélie
4273 m
WT, WL
Cave T & P
Adélie Entrance
Guide Rocks Entrance
4310 m
N T
Subway Entrance
Climbers Refuge Entrance
Legend
Slope
Ice wall
Ice wall - Estimated
Ice
Dangerous Atmosphere
Entrance/Drip line
Water
Fumarole
Cartography: Christian Stenner & David A. Riggs

Figure 2.


A
B
C
PETZL

Figure 3.

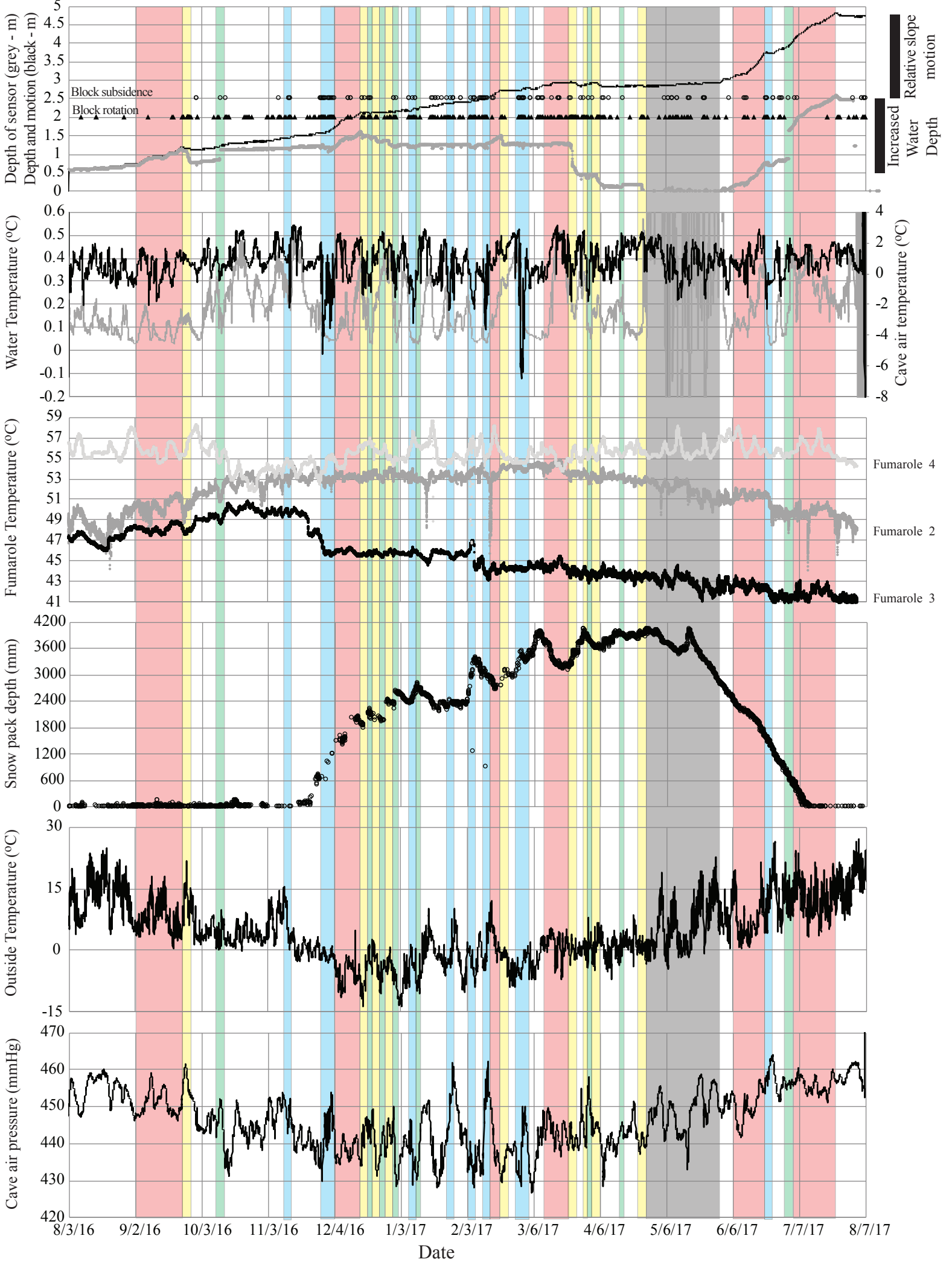
Depth of sensor (grey - m)
Depth and motion (black - m)
Block subsidence
Block rotation
Relative slope motion
Increased Water Depth
Water Temperature (ºC)
Cave air temperature (ºC)
Fumarole Temperature (ºC)
Fumarole 4
Fumarole 2
Fumarole 3
Snow pack depth (mm)
Outside Temperature (ºC)
Cave air pressure (mmHg)
8/3/16
9/2/16
10/3/16
11/3/16
12/4/16
1/3/17
2/3/17
3/6/17
4/6/17
5/6/17
6/6/17
7/7/17
8/7/17
Date

Figure 4.

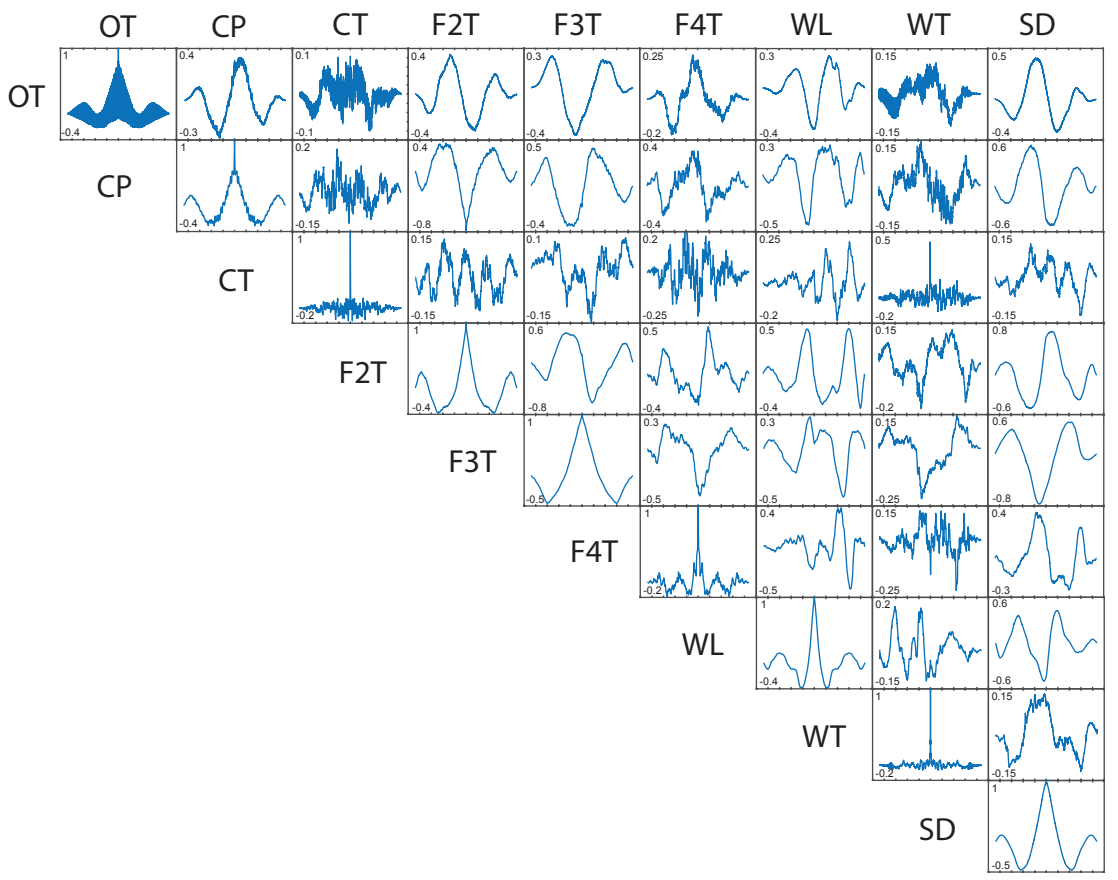
OT
CP
CT
F2T
F3T
F4T
WL
WT
SD

Figure 5.

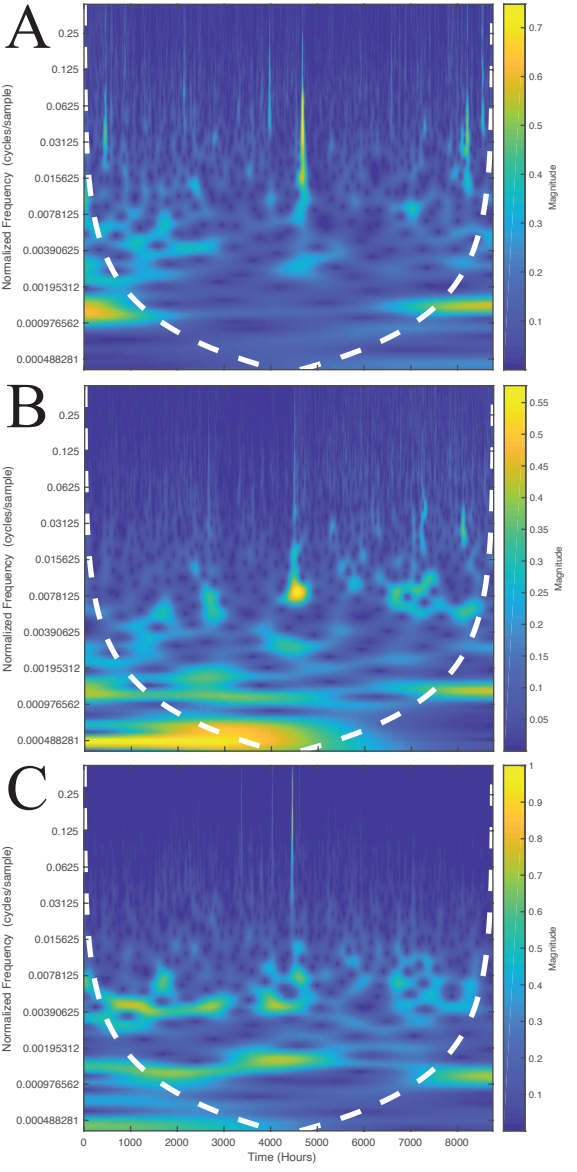
A
B
C
Normalized Frequency (cycles/sample)
0.25
0.125
0.0625
0.03125
0.015625
0.0078125
0.00390625
0.00195312
0.000976562
0.000488281
Magnitude
0.7
0.6
0.5
0.4
0.3
0.2
0.1
0.55
0.45
0.35
0.25
0.15
0.05
1
0.9
0.8
0.7
0.6
0.5
0.4
0.3
0.2
0.1
0
1000
2000
3000
4000
5000
6000
7000
8000
Time (Hours)

Figure 6.

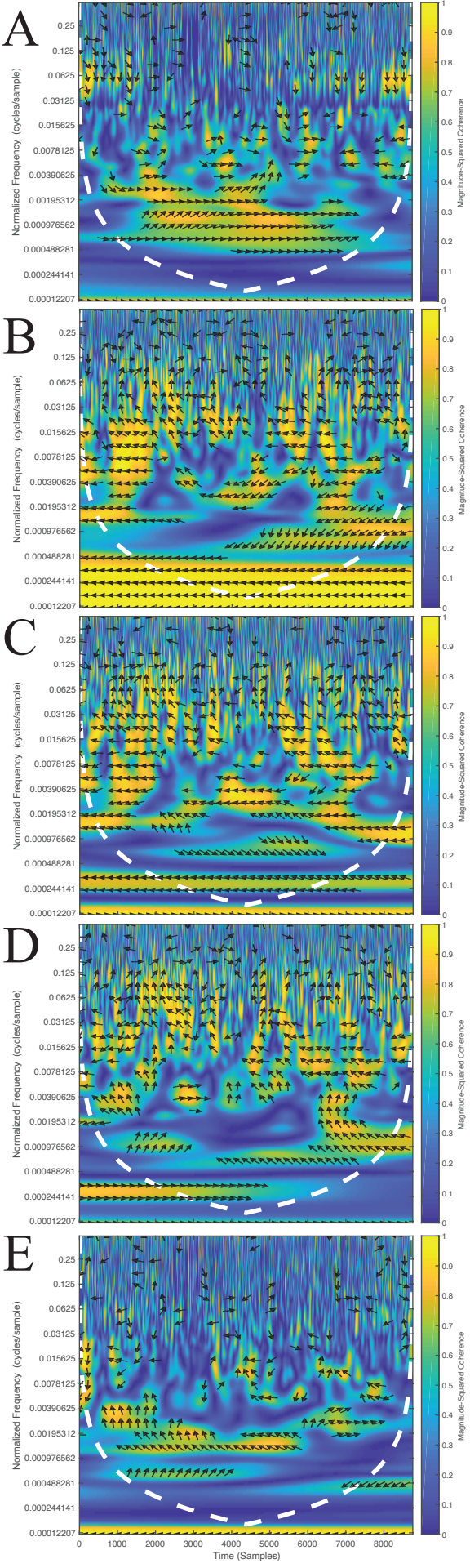
A
B
C
D
E
Normalized Frequency (cycles/sample)
0.25
0.125
0.0625
0.03125
0.015625
0.0078125
0.00390625
0.00195312
0.000976562
0.000488281
0.000244141
0.00012207
Magnitude-Squared Coherence
0
0.1
0.2
0.3
0.4
0.5
0.6
0.7
0.8
0.9
1
0
1000
2000
3000
4000
5000
6000
7000
8000
Time (Samples)

Figure 7.

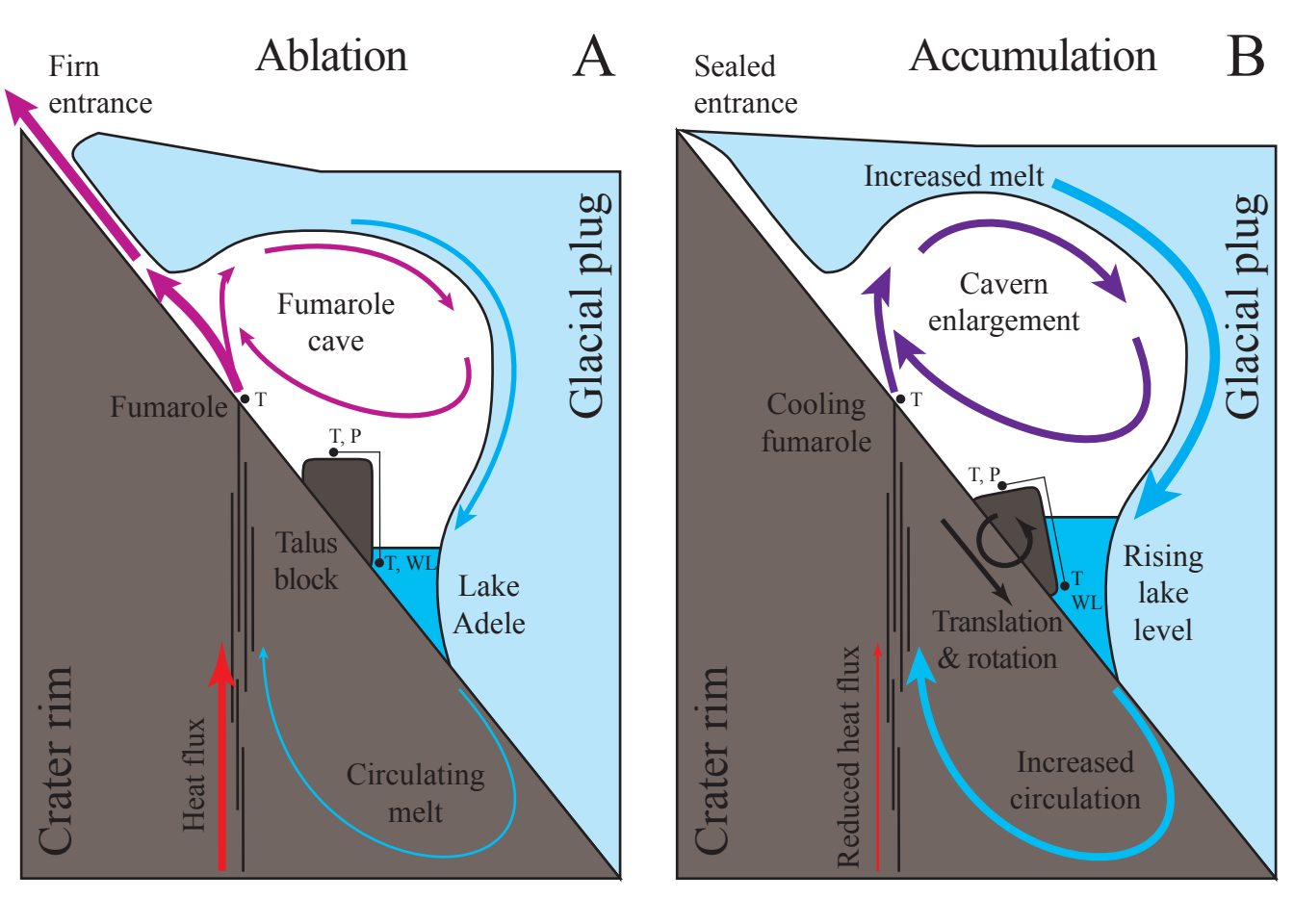
Ablation
A
Firn
entrance
Fumarole
cave
Fumarole
T
T, P
Talus
block
T, WL
Lake
Adele
Glacial plug
Crater rim
Heat flux
Circulating
melt
Accumulation
B
Sealed
entrance
Increased melt
Cavern
enlargement
Cooling
fumarole
T
T, P
T
WL
Rising
lake
level
Translation
& rotation
Glacial plug
Crater rim
Reduced heat flux
Increased
circulation